

In Situ Activation of Snap-Through Instability in Multi-Response Metamaterials through Multistable Topological Transformation

Lei Wu and Damiano Pasini*

Snap-through instability has been widely leveraged in metamaterials to attain non-monotonic responses for a specific subset of applications where conventional monotonic materials fail to perform. In the remaining more plentiful set of ordinary applications, snap-through instability is harmful, and current snapping metamaterials become inadequate because their capacity to snap cannot be suppressed post-fabrication. Here, a class of topology-transformable metamaterials is introduced to enable in situ activation and deactivation of the snapping capacity, providing a remarkable level of versatility in switching between responses from monotonic to monostable and bistable snap-through. Theoretical analysis, numerical simulations, and experiments are combined to unveil the role played by contact in the topological transformation capable of increasing the geometry incompatibility and confinement stiffness of selected architectural members. The strategy here presented for post-fabrication reprogrammability of matter and on-the-fly response switching paves the way to multifunctionality for application in multiple sectors from mechanical logic gates, and adjustable energy dissipators, to in situ adaptable sport equipment.

capacity^[10] or bearing extremely large tension strain.^[11] Bistable snapping in metamaterials finds a wide range of applications such as energy trapping,^[12–15] mechanical signal propagation with high fidelity,^[16–18] multistable shape reconfiguration,^[19,20] reprogrammable mechanical memory,^[21] and mechanical logic operations,^[22–24] among several others. The response of a mechanical metamaterial is mainly governed by the structural characteristics of its architecture besides the properties of its constituent solids.^[11] One key strategy to attain snap-through instability is to rationally design the metamaterial architecture, which can span a wide range of structural concepts, from the von Mises Truss,^[25,26] inclined or curved beams,^[10,11,13] shells and domes,^[27,28] to origami and kirigami.^[24,29–32] Existing works have so far focused on harnessing the negative incremental stiffness provided by these structural concepts to endow a metamaterial with distinct functionalities


1. Introduction

Snap-through instability is a limit-point buckling phenomenon in a system with negative incremental stiffness.^[1,2] It can be witnessed across the length scale spectrum in both the technological and biological worlds, from aircraft panels^[3] and microelectromechanical devices,^[4] to the Venus flytrap.^[5] Snap-through instability can be classified as either monostable or bistable, and in recent years, it has been embedded into metamaterials to attain unprecedented responses.^[6–9] Monostable snapping can be harnessed to design metamaterials with reusable energy dissipation

at the concept stage of design. Once manufactured, however, their as-built architecture is permanently imprinted with snap-through characteristics that cannot be changed in service through a mechanical input unless a field-responsive material is used and triggered by the application of an external physical field, such as a thermal or electromagnetic stimulus.^[21,33,34] As a result, current concepts that do not rely on a physical stimulus cannot switch their mechanical response in situ, for example from snap-through to monotonic, because their snap-through instability cannot be intrinsically deactivated post-fabrication. This immutability prevents them from behaving as conventional materials delivering a monotonic stress-strain relation, and from using them in a multitude—even larger—spectrum of ordinary applications where snapping instabilities are detrimental. One example of the latter is in applications requiring a high force-transmittance at large strain, a scenario where snapping materials show their weakness. In-situ invariability of mechanical response is thus a critical bottleneck to fully tap into multi-functionality.

In this work, we propose a class of topology-transformable metamaterials that can deliver post-fabrication a remarkably diverse set of mechanical responses, including monotonic, monostable snap-through, and bistable snap-through. By reprogramming in situ selected architectural constituents, a process de-

L. Wu, D. Pasini
Department of Mechanical Engineering
McGill University
Montreal Quebec H3A 0C3, Canada
E-mail: damiano.pasini@mcgill.ca

 The ORCID identification number(s) for the author(s) of this article can be found under <https://doi.org/10.1002/adma.202301109>

© 2023 The Authors. Advanced Materials published by Wiley-VCH GmbH. This is an open access article under the terms of the Creative Commons Attribution License, which permits use, distribution and reproduction in any medium, provided the original work is properly cited.

DOI: 10.1002/adma.202301109

noted as *activation process*, we can on demand turn on and off snap-through instabilities along one principal direction by switching the state of the metamaterial along the other principal axes. To attain this goal, we first introduce a multi-body model that can realize the activation process through a contact-induced topological transformation. After unveiling the enabling mechanism, we leverage the multi-body model to propose a 2D metamaterial that can switch responses between monotonic and snap-through, and demonstrate its application for a novel snapping-based mechanical logic gate in a motion-transmission system. We then extend the 2D concept to three-dimension to realize a spatial multi-response metamaterial with activatable snap-through instability that can integrate monotonic, monostable snap-through, and bistable snap-through within a single architecture.

2. Multi-Body Architecture with Reprogrammable Snap-Through Instability

A paradigmatic concept for achieving snap-through instability is the von Mises truss, a V-shape framework comprising two inclined trusses with a rotational spring (k_r) at its apex and two ends confined between grounded springs k (Figure 1a-i).^[25,26,35] The von Mises truss can exhibit three types of force–displacement response (Figure 1a-ii): monotonic response with no stationary points, monostable snap-through that has two positive stationary points, and bistable snap-through with one positive and one negative stationary point.^[25] All these responses are governed by two non-dimensional parameters, θ/π , that is, the inclination angle denoted as the degree of geometry incompatibility,^[36] and kl^2/k_r (Figure 1a-i), the confinement stiffness provided to the inclined members.^[37] Figure 1a-iii shows a phase diagram depicting the change in the von Mises truss response with varying values of θ/π and kl^2/k_r . The three domains highlight the interplay between geometry incompatibility and confinement stiffness in attaining a given type of response; the higher their values, the easier is to access snap-through regions (either monostable or bistable). To date, once fabricated, metamaterials using the von Mises Truss can deliver only one single response among the three.

To integrate monotonic (positive incremental stiffness) and snapping (negative incremental stiffness) responses into one in-situ transformable architecture, we follow a bottom-up strategy from the 2D building block up to the 3D architecture. Our rationale is to pair a von Mises truss with a monotonic response with another von Mises truss that is bistable such that the geometry incompatibility of the former can be reprogrammed by altering the state of the latter. Figure 1b-i shows our enabling concept, a multi-body architecture with interacting rigid and deformable elements. It features two inclined rigid truss elements (AB and CD) connected by a short rigid bar (BC), which is coupled to an elastic Timoshenko beam (yellow rectangle BCEF) having its side EF grounded. The elastic Timoshenko beam provides confinement to both the inclined truss elements AB and CD. In other words, the truss elements AB and CD can interact via the elastic Timoshenko beam. AB is selected as the bistable truss element and CD as the monotonic one. The aspect ratio (edge BF length over edge BC length) of the Timoshenko beam is selected as 26/11 (Figure S1, Supporting Information), a value endowing

the beam stiffness a trade-off. On one hand, it can provide sufficient confinement for the truss element AB to attain bistability; on the other hand, it does not generate an overly stiff beam, which would spoil the kinematic role of the elastic connector providing the necessary coupling between the truss elements, AB and CD. To ensure the bistability of the truss element AB while avoiding a too-high energy barrier for state transition, we select an appropriate value for the geometry incompatibility, that is, $\theta_1 = 33.2^\circ$ (Figure S1, Supporting Information). As per the truss element CD, we set $\theta_2 = 6.6^\circ$ (Figure S1, Supporting Information) to ensure the monotonicity of its response. A theoretical model is also developed to investigate the bistable transition of the truss element AB, and the γ -response of the truss element CD (Section S1, Supporting Information). After a cycle of compression and decompression in the x -direction (Figure 1b-ii), a process denoted hereafter as the *activation process*, the architecture transitions to its second stable state with self-stress. Due to the activation, the Timoshenko beam has slightly bent, the truss element AB has become reentrant, and the truss element CD has gained a larger inclination angle compared to θ_2 in its initial state. Upon activation, we apply at node D a downward force, F_y , to investigate the force–displacement relation in the γ -direction (see inset in Figure 1b-iii and Section SI, Supporting Information). Prior to activation, the system response in the γ -direction is monotonic due to the intentionally adopted low geometry incompatibility $\theta_2 = 6.6^\circ$ (green curve in Figure 1b-iii). In contrast, the activated architecture exhibits a conspicuous snap-through behavior (purple curve in Figure 1b-iii) due to the enhanced geometry incompatibility of the truss element CD. Nevertheless, the snap-through in the γ -direction is still monostable. This outcome is due to the reconfiguration from Figure 1b-i to Figure 1b-ii, a process that increases θ_2 to a certain extent, but it has only a limited impact on the confinement stiffness for the truss element CD, which is provided by the bending stiffness of the rectangle BCEF.

To change the γ -direction response of the activated architecture in Figure 1b-ii from monostable snapping to bistable snapping, we learn from Figure 1a-iii that we need to further enhance the geometry incompatibility and confinement stiffness, that is, the bending stiffness of the beam BCEF. To this end, we replace the truss elements AB, BC, and CD in Figure 1b with rigid triangles and then mirror them with respect to two orthogonal axes so as to obtain a 2D building block with reflection symmetry (Figure 1c). This mirror operation seeks to generate a symmetric architecture and enable compatible contact between pairing edges (e.g., AG and AG') in the activated state (Figure 1d-i), which can lead to a topological transformation^[38,39] capable of enhancing the geometry incompatibility of the triangle CDH and the confinement stiffness for the triangle CDH. Topology is here defined in the physical space and refers to the nodal/edge connectivity of the material architecture, for example, the number of elements that meet at a given node or edge. The merging of edges and nodes that takes place during the reconfiguration due to contact attests that our metamaterial undergoes a topological transformation.

Contact plays a major role in the response of our architecture. Whether contact is established in the activated state is mainly dictated by α , the spacing angle between pairing edges. There exist bounds for α that govern the establishment of contact, and that we now determine. If we alter α by rotating the edge AG with respect to node A (see the right-hand side of Figure 1c), there

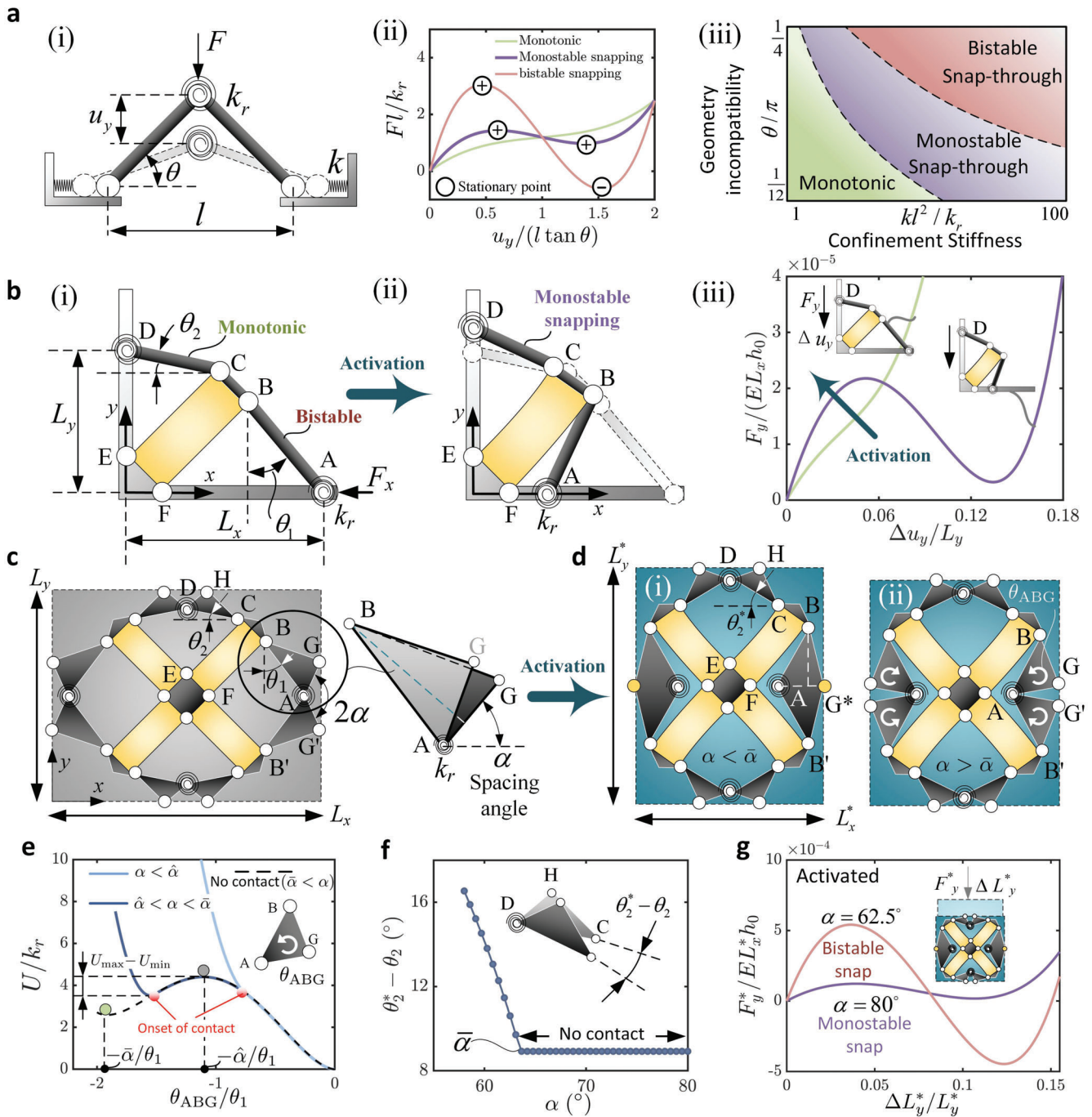


Figure 1. a) Schematic diagram of the von Mises Truss (i), three representative types of force–displacement response (ii), and phase diagram (iii) depicting the interplay between geometry incompatibility (θ/π) and confinement stiffness (kl^2/k_r) in governing the type of response. b) Multi-body system consisting of three bars (black) and a deformable body (yellow) prior to (i) and post (ii) activation through in situ application of F_x , where $\theta_1 = 33.2^\circ$ and $\theta_2 = 6.6^\circ$ (see Figure S1, Supporting Information, for assessment of angle values); (iii) prior to activation, the y -response is monotonic (green curve), while it becomes monostable snap-through (purple curve) once the system is activated; the y -axis is the normalized force, where $E = 146.0$ MPa is the Young's modulus of the Timoshenko beam BCEF, and $h_0 = 30.0$ mm is the out-of-plane thickness (Sections S1 and SV, Supporting Information). c) Multi-body unit cell architecture and key geometry parameters. d) Activated configuration either with contact-induced topological transformation (i) or without (ii). e) Energy landscape during activation, where U is the strain energy of a quarter of the unit cell; 3 curves, each representing a type of contact onset, are plotted. f) Relationship between spacing angle α and increased geometry incompatibility ($\theta_2^* - \theta_2$); a change of α does not affect $\theta_2^* - \theta_2$ if $\alpha > \bar{\alpha} \approx 63.6^\circ$. g) Two representative responses of activated architecture with $\alpha = 62.5^\circ$ (bistable snapping) and $\alpha = 80.0^\circ$ (monostable snapping).

exists a critical value $\bar{\alpha}$ for the spacing angle α , beyond which there is no contact in the activated state (Figure 1d-ii), since the triangle ABG has a sufficiently large spacing angle to rotate without touching its mirrored part (AB'G'). By inspecting the normalized energy landscape of the architecture during activation (Figure 1e), we observe that $\bar{\alpha}$ corresponds to the local minimum point of the energy curve (green spot defined by $\partial U/\partial\alpha_{\alpha=\bar{\alpha}} = 0$ and $\partial^2 U/\partial\alpha_{\alpha=\bar{\alpha}}^2 > 0$ on the dashed curve in Figure 1e), where internal contact is neglected. $\bar{\alpha}$ has a value that is slightly lower than $2\theta_1$ due to the non-negligible rotational stiffness of the hinge; from our theoretical analysis, we obtain $\bar{\alpha} \approx 1.9\theta_1$. On the other hand, there exists another critical value $\hat{\alpha}$ for the spacing angle α , below which the contact takes place prior to the local maximum point (grey spot defined by $\partial U/\partial\alpha_{\alpha=\hat{\alpha}} = 0$ and $\partial^2 U/\partial\alpha_{\alpha=\hat{\alpha}}^2 < 0$ on the dashed curve in Figure 1e). This contact occurs too early; it reshapes the originally double-well curve to a convex curve (light blue curve in Figure 1e) and hence undermines the bistable activation. From our theoretical model, we obtain that $\hat{\alpha} \approx 1.1\theta_1$. In the case of $\hat{\alpha} < \alpha < \bar{\alpha}$, we can observe contact in the activated state (dark blue curve in Figure 1e), where the triangles ABG and AB'G' join their side via interface compression,^[38] and the nodes G and G' merge into a new pivot G* (Figure 1d-i). The existence of contact brings a topological transformation,^[38] which has two salient features. First, it can increase the distortion of the beam BCEF, hence further improving the geometry incompatibility of the triangle CDH (θ_2^*) in the activated state. Second, the newly merged body ABG*B' can through interface contact prevent the Timoshenko beam BCEF from bending, thus enhancing the confinement stiffness for the triangle CDH. Both these outcomes are instrumental to reaching the goal of obtaining bistability in the y -direction. In summary, the analysis above shows that $\hat{\alpha}$ and $\bar{\alpha}$ divide the design space of the spacing angle α into to 3 regimes, that is, $\alpha < \hat{\alpha}$, $\hat{\alpha} < \alpha < \bar{\alpha}$, and $\bar{\alpha} < \alpha$; the former should be excluded because it cannot yield bistable activation. An additional design requirement concerns the selection of a spacing angle α that provides a robust activated state, denoted as $U_{\max} - U_{\min}$ (Figure 1e). To this end, we observe that the onset of contact (red spot in Figure 1e) should appear at a position sufficiently apart from the left of the local maximum point. This choice results in a comparably higher $U_{\max} - U_{\min}$, which in turn ensures the robustness of the activated state. With the insights above, we can select a spacing angle range of $\alpha \in [58.0^\circ, 80.0^\circ]$, where $58.0^\circ > \hat{\alpha}$ enables a robust activated state, and $80.0^\circ > \bar{\alpha}$ ensures that both contact and non-contact cases are covered.

The next step is to investigate the role of geometric incompatibility in the activated configuration and the y -response post-activation (Section SI, Supporting Information). As explained above, the activation accompanied by internal contact can facilitate the geometry incompatibility of the triangle CDH. We parametrically study how the boost of the geometry incompatibility of the triangle CDH, denoted as $\theta_2^* - \theta_2$, evolves with the spacing angle α , as shown in Figure 1f. As α rises, $\theta_2^* - \theta_2$ gradually decreases since a higher spacing angle α reduces the height of the triangle ABG (see the dashed line on the right of Figure 1c), which is in a positive relationship with θ_2^* (Figure 1d-i). When α reaches $\bar{\alpha}$, $\theta_2^* - \theta_2$ drops to a lower bound, and a further increase of α would not alter $\theta_2^* - \theta_2$ since there is no edge contact in the initial configuration of the activated architecture due to the large spacing angle α . The lower bound of $\theta_2^* - \theta_2$ is governed

by the rotational stiffness of the hinge, θ_1 , θ_2 , the dimensions of the Timoshenko beam, and the base material properties; in other words, this lower bound corresponds to the second stable configuration of the architecture in the absence of any internal contact (green spot in Figure 1e). To attain a bistable snap-through in the activated state, a sufficiently high geometry incompatibility θ_2^* is needed, and hence we should select a relatively small α such as $\alpha = 62.5^\circ$; Figure 1g shows the corresponding force-displacement relation with the bistable curve in red. On the other hand, if the target is to obtain a monostable snapping response post-activation, a comparably small geometry incompatibility θ_2^* is needed, which can be achieved by selecting a large α , such as $\alpha = 80.0^\circ$; this weakens the action of contact and imparts a monostable snapping response to the activated system (purple curve in Figure 1g).

3. Dual-Response 2D Metamaterial

After unveiling the activation mechanism of contact-induced topological transformation, we use the multi-body architecture of Figure 1c to develop a 2D monolithic metamaterial capable of switching its response between monotonic and snap-through. Figure 2a-i shows a representative unit cell where the rotating triangles, for example, ABG and CDH, can deform only slightly, hence mainly undergoing rigid-body motion. The rectangular beam BCEF can undergo finite bending and thus act as a communicator that couples the motion of the triangles ABG and CDH. From our previous analysis, to guarantee the activability (bistability) in the x -direction, we need to adopt $\theta_1 = 37.0^\circ$, and to ensure that the unit cell prior to activation shows a monotonic response in the y -direction, we set $\theta_2 = 7.5^\circ$ (additional details on geometry parameters in Figure S4, Supporting Information). We point out that the values of θ_1 and θ_2 in the ideal multi-body architecture slightly differ from those of the monolithic model due to the non-negligible size of the living hinge.

Since the spacing angle α governs the contact behavior of the multi-body architecture and the response post-activation, we now assess its role on the monolithic model. To do so, we numerically investigate via the Finite Element (FE) method how the stress-strain relation of the material (y -direction) evolves with α . The initial geometry incompatibility of the triangle CDH (θ_2) is prescribed at 7.5° , and the spacing angle α is swept from 58.0° to 80.0° (Section SII and Movie S1, Supporting Information). The constituent material is Thermoplastic Polyurethane (TPU) with a linear elastic modulus of 146.0 MPa, a Poisson's ratio of 0.47, and mass density of $1158.6 \text{ kg}\cdot\text{m}^{-3}$ (Section SV, Supporting Information). In our analysis, σ_y and ϵ_y correspond to the nominal compression stress and strain in the y -direction respectively. Prior to activation, the σ_y - ϵ_y relation is monotonic for $\alpha \in [58.0^\circ, 80.0^\circ]$; a change in α has only a minor outcome on the σ_y - ϵ_y relation since there is no contact taking place during loading (green curves in Figure 2b). Upon activation, the metamaterial response becomes more sensitive to α due to the presence of contact (topological transformation). Similar to the multi-body architecture (Figure 1c), the activated metamaterial shows snap-through instability and transitions from bistable (red curves in Figure 2a-ii) to monostable (purple curves in Figure 2a-ii) as α increases.

To determine the critical value of α that separates the bistable and monostable regimes, we can monitor $\sigma_{\min}/\sigma_{\max}$ (bottom of

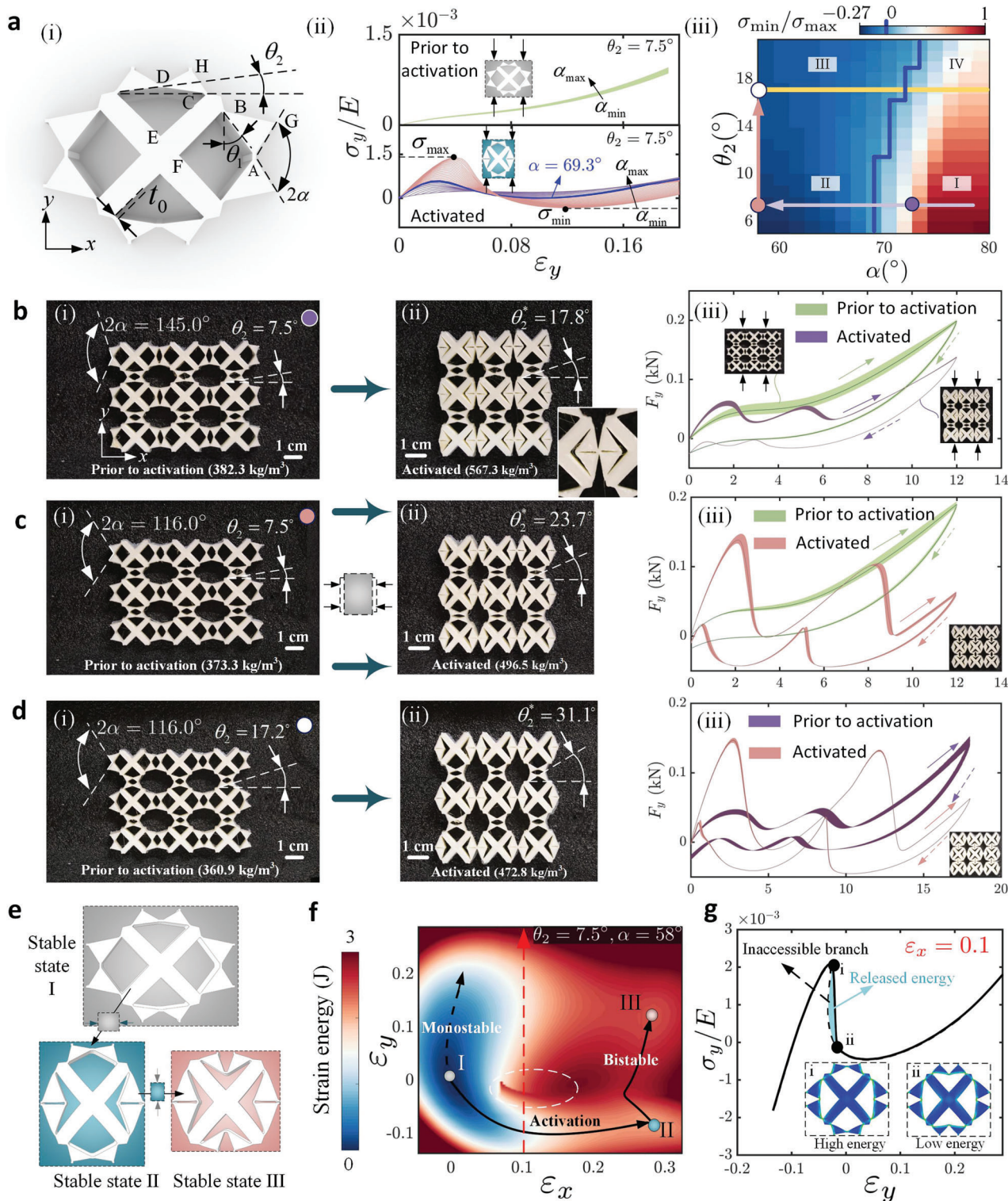


Figure 2. a) Unit cell of dual-response 2D metamaterial with $t_0=1$ mm hinge thickness and $h_0=30$ mm out-of-plane thickness (i); Numerically-obtained σ_y - ϵ_y relation prior to (top row) and post-activation (bottom row), where $\theta_2 = 7.5^\circ$ (ii); contour plot of $\sigma_{\min}/\sigma_{\max}$ in the θ_2 - α space, which defines 4 sub-regions, each corresponding to one type of activation processes (iii). Finite-period tessellations demonstrating the transition from b) monotonic to monostable snapping, c) monotonic to bistable snapping, and d) monostable snapping to bistable snapping, in which the right-bottom insets in (iii) illustrate the fully condensed stable state of the samples. e) Three stable states of the unit cell in (c). f) Strain energy landscape of the unit cell the ϵ_x - ϵ_y space; solid arrows indicate bistable transitions. g) Snap-back instability of the unit cell for given $\epsilon_x = 0.1$, visualized by the red dashed arrow in (f); insets i and ii illustrate the configurations of the unit cell before and after the snap-back event.

Figure 2a-ii) versus α . The σ_y - ϵ_y curve with $\sigma_{\min}/\sigma_{\max} = 0.0$ indicates the critical case, where the local minimum just takes place at a zero point of the curve. In our analysis, we numerically find that $\alpha = 69.3^\circ$ yields $\sigma_{\min}/\sigma_{\max}$ approaching null, as highlighted in blue in Figure 2a-ii. This critical value of the spacing angle can be altered if we change the initial geometry incompatibility of the triangle CDH, that is, θ_2 (see Section SII, Supporting Information for details). A parametric study in the design space of $\theta_2 \in [5.1^\circ, 21.3^\circ]$ and $\alpha \in [58.0^\circ, 80.0^\circ]$ allows to generate the contour plot of $\sigma_{\min}/\sigma_{\max}$ post-activation, which is shown in Figure 2a-iii. In the region right to the blue boundary in Figure 2a-iii, $\sigma_{\min}/\sigma_{\max} > 0.0$, which corresponds to a monostable snapping response. In the region left to the blue boundary, $\sigma_{\min}/\sigma_{\max} < 0.0$, and the metamaterial post-activation is bistable. As θ_2 increases, the blue boundary (critical value of α to ensure bistability) shifts rightward; this indicates that even with a relatively large spacing angle α , the metamaterial having an initially higher geometry incompatibility θ_2 can still be bistable. On the other hand, the yellow boundary in Figure 2a-iii separates the pre-activation response into two, namely monotonic (lower part) and monostable snapping (upper part). Since the spacing angle α has very minor effect on the pre-activation response, the yellow boundary is a horizontal line, which we obtain by sweeping θ_2 for prescribed α (Section SII, Supporting Information). The two boundaries divide the design space into 4 sub-regions, where regions I, II, III, and IV respectively correspond to a transition from: i) monotonic (prior to activation) to monostable snapping (post-activation), ii) monotonic to bistable snapping, iii) monostable snapping to bistable snapping, and iv) monostable snapping to enhanced monostable snapping.

From the numerical results, we select representative finite-period specimens for fabrication (Section SIII, Supporting Information) and demonstrate their ability to reversibly switch their response on the fly from monotonic (prior to activation) to monostable and bistable snap-through (post-activation). Illustrated in Figure 2b are (i) a truncated 3×3 structure tessellated by a unit cell with $\theta_2 = 7.5^\circ$ and $\alpha = 72.5^\circ$, which refers to the purple spot in Figure 2a-iii, (ii) its fully activated configuration, and (iii) the corresponding stress-strain curves in the inactive/activated states. The activation brings about a contact-induced topological transformation (see the inset in Figure 2b-ii) that enhances the geometry incompatibility from 7.5° to 17.8° , thereby triggering the monostable snap-through instability (purple curve in Figure 2b-iii and Movie S2, Supporting Information). As indicated by the light purple arrow in Figure 2a-iii, a gradual reduction of the spacing angle α for prescribed θ_2 progressively enhances the extent of snap-through post-activation while keeping the response prior to activation monotonic. This is demonstrated through a set of uniaxial compression tests for $\alpha = 77.5^\circ$, 67.5° , 62.5° , and 58.0° (see Section SIII, Supporting Information). Dealing with as-built architecture raises the issue of imperfections induced by manufacturing and their role in attaining robust bistability post-activation. To compensate for their influence as well as for the viscoelasticity of the base material, we select a spacing angle α that is moderately lower than that obtained via FE analysis for an ideal architecture ($\alpha = 69.3^\circ$). In Figure 2c, we demonstrate the case for $\alpha = 58.0^\circ$, which corresponds to the light red spot in Figure 2a-iii. For $\alpha = 58.0^\circ$, the activation can improve the geometry incompatibility θ_2 from 7.5°

(Figure 2c-i) to 23.7° (Figure 2c-ii), hence facilitating a bistable response post-activation (red curve in Figure 2c-iii). Owing to the viscoelasticity of the base material,^[40] the loading branch of the red bistable curve in Figure 2c-iii does not show a significant negative value even though it crosses the zero-force horizon. Unlike other pseudo-bistable structures with viscoelasticity that can only retain the reconfigured shape for a certain period of time,^[41,42] our sample can robustly preserve its reconfigured shape even under moderate perturbations (Movie S3, Supporting Information).

Besides the activation from monotonic to snap-through, we can also reprogram the type of snap-through, that is, achieving a transition from monostable snap-through to bistable snap-through. To this end, we follow the light red arrow in Figure 2a-iii and gradually increase θ_2 while keeping $\alpha = 58.0^\circ$ to reach region III in Figure 2a-iii (from monostable snapping to bistable snapping). A set of compression tests on finite structures with $\theta_2 = 10.0^\circ$, 12.5° , 14.9° , and 17.2° are performed (Figure S10 and Section SIII, Supporting Information). In experiments, we found that due to the softening behavior of the base material (Thermoplastic Polyurethane) at a finite strain, a geometry incompatibility $\theta_2 = 17.2^\circ$ (white spot on the yellow boundary in Figure 2a-iii) can provide an evident monostable snapping response prior to activation; its force–displacement curve is thus plotted in purple in Figure 2d-iii. Post-activation, the topological transformation further enhances the metamaterial's geometry incompatibility (Figure 2d-ii), thus upgrading the snap-through from monostable to bistable (red curve in Figure 2d-iii and Movie S4, Supporting Information). While a transition from monostable snapping to bistable snapping can be found in a few recent works,^[22,37] their transition is only temporary, whereas our concept can provide a robust and stationary activation.

In addition to the investigation of 0% and 100% activation applied to the finite-period structures shown in Figure 2, we also experimentally investigate their responses in a partially activated state, where only a selected portion of the building blocks are activated (see force–displacement curves in Figures S11–S13, Supporting Information). By progressively increasing the percentage of activation, the resulting heterogeneous finite structures globally exhibit a gradual boost of snap-through instability, a phenomenon further signifying the remarkable reprogrammability of our metamaterial. In particular, the finite structure with $\theta_2 = 7.5^\circ$ and $\alpha = 58.0^\circ$, can exhibit a monotonic, a monostable snap-through, and a bistable snap-through response respectively under 0%, 67%, and 100% of state activation.

The activation mechanism from monostability to bistability of the metamaterial in Figure 2c can be also elucidated from the study of the energy landscape of its unit cell (Section SII, Supporting Information). The unit cell in Figure 2c has three distinct stable states: the free-stress state (state I in Figure 2e), the activated state (state II in Figure 2e), and the fully condensed state (state III in Figure 2e). As a result, there exist three local minimum points on the strain-energy plot (Figure 2f). Deforming the unit cell can be thought of as analogous to moving a ball on the energy surface. If we start with the state I and apply a force in the y -direction, the ball follows the dashed path (Figure 2f) to climb the mountain. Given this path does not point to a local minimum point, the ball returns to its initial position upon the removal of the applied force, and hence the unit cell is monostable. However, if we first apply a force in the x -direction, which corresponds to

the activation process, the ball follows the solid path (Figure 2f) and reaches the local minimum point II. A subsequent application of a force in the y -direction can transition the ball from state II to state III, that is, the activated unit cell has become bistable in the y -direction. From an energetic standpoint, the mechanism for activating bistability is equivalent to transitioning the metamaterial from the zero-energy state to a high-energy intermediate state that is activated and adjacent to the final state.

In the strain energy landscape, ϵ_x - ϵ_y space, we point out the existence of discontinuity at certain locations. These define a region (white dashed circle in Figure 2f) that corresponds to some highly incompatible configurations of the unit cell, where the rotational triangles are close to their unstable equilibrium state (e.g., insets i and ii in Figure 2g). Crossing this incompatible region with a strain/displacement-controlled load can result in snap-back instability, a phenomenon during which a portion of the stored strain energy is released, hence leading to energy discontinuity. An instance of crossing this region is shown by the dashed red arrow in Figure 2f, and its corresponding σ_y - ϵ_y relation for prescribed $\epsilon_x = 0.1$ is plotted in Figure 2g. A sudden drop of σ_y at given ϵ_y , that is, snap-back instability, is associated with a release of energy (light blue area). The snap-back phenomenon indicates that under an identical strain state, there exists one high-energy configuration (inset i in Figure 2g) and one low-energy configuration (inset ii in Figure 2g). Which configuration between the two we reach, depends on the loading history. We also emphasize that to access this incompatible region a fairly high input energy is required, hence snap-back does not affect our activation process and the y -response post-activation.

4. Application as Mechanical Logic Gates

Since the bistability of our metamaterial in one direction is governed by the state (topology) in the other direction, one natural application to showcase this functionality is for the design of mechanical logic gates. Compared to conventional electronic logic gates, their mechanical counterparts can more robustly resist harsh environments subjected for instance to strong electromagnetic radiation; they can thus appeal to space engineering applications involving system control. Here we demonstrate that our concept can achieve the basic logic gates functions and be used as a mechanical conductor or breaker that can deliver or stop displacement loading in a motion-transmission system. One key difference between the conventional mechanical logic gates in literature and the logic gates we present here is that the output of existing gates is the displacement amplitude,^[16,43,44] whereas ours outputs the monostability/bistability, that is, whether the output architecture can snap to its second stable state if there exists. This is a key difference indicating that the output of our mechanical logic gate is in principle non-volatile, that is, the output property is robustly preserved even if there exist perturbations on the output end.

Figure 3a illustrates a mechanical “AND” gate consisting of two identical bistable architectures (within the blue dashed box) working as two independent inputs, where the open/inactive state corresponds to “0”, and the activated (condensed) state corresponds to “1”. In the red dashed box is the output archi-

ture with an inclination angle of θ_2 . The input and output parts are coupled by a deformable cross-type architecture. For an “AND” gate, a relatively small θ_2 is preferred, for example $\theta_2 = 10.0^\circ$, such that the output architecture is initially monostable but can become bistable if - and only if - both inputs are activated (Figure 3a and Movie S5, Supporting Information). Using the “AND” gate and rationally tuning the relevant geometry parameters, we can obtain the other 3 basic logic gates (Figures S18 and S19, Supporting Information).

An increase of θ_2 in the “AND” gate can yield an “OR” gate. For instance, for $\theta_2 = 19.5^\circ$, the output architecture is monostable if the input is “00”; however, once there has been at least one side activated (input is either “01”, “10”, or “11”), the resulting high geometry incompatibility is sufficient to empower the output architecture with bistability (Figure 3b and Movie S5, Supporting Information). The “OR” gate can be further modified by assigning $\gamma = 0.0^\circ$ and keeping $\theta_2 = 19.5^\circ$ to derive an “XOR” gate. A parametric study mapping the role of γ in the post-activation response is given in Section SII (Supporting Information). The logic operation (mechanical response) of the “XOR” gate is similar to that of the “OR” gate when the input is “00”, “01”, or “10”. Nevertheless, when both two sides are activated, that is, the input is “11”, the resulting output architecture shows a negative γ (inset of Figure 3c in the top-right corner). In this case, when we compress the output architecture, the triangles CDH and C'DH' rotate outward as opposed to inward, hence being unable to snap to the second stable state and resulting in a monostable output architecture. Next, if we increase θ_2 to $\theta_2 = 35.3^\circ$ in the “XOR” gate, and keep $\gamma = 0.0^\circ$, we can derive a “NAND” gate. Initially bistable under compression, the output architecture of the “NAND” gate can become monostable if - and only if - both two sides are activated (Figure 3d) due to the existence of a negative γ post-activation. A detailed explanation of the impact of γ in the “XOR” and “NAND” gates is illustrated in Figure 3e by a simplified rigid-body model, where the two linear springs represent the deformable cross-type architecture of the physical model. If the input is “00”, the edges CH and C'H' are vertical, and the applied compression forces are collinear with these two edges. Due to the non-negligible size of the hinges C and C', the triangles CDH and C'DH' tend to rotate inward to undergo snapping (left side of Figure 3e). If the input is “11”, the edge CH/C'H' experiences a clockwise/counterclockwise rotation. As a result, the applied compression force generates a moment about the hinge C/C' that rotates the triangle CDH/C'DH' clockwise/counterclockwise, thus preventing the output architecture from transitioning to its second stable state (right side of Figure 3e).

The results of the analysis above show that our mechanical logic gates can sense two displacement signals and then adjust their response to function as a mechanical breaker (bistable) or conductor (monostable). These functionalities can either halt or enable the motion transmission once the displacement load exceeds a threshold value. We now demonstrate the use of the “NAND” gate as an instance. We consider a motion-transmission system comprising a loading head, an elastic component, here represented by an elastic beam lying on two rigid supports, a target object (white egg) that is underneath the elastic component, and a “NAND” gate that lies between the loading head and the elastic component (Figure 3f-i). A downward displace-

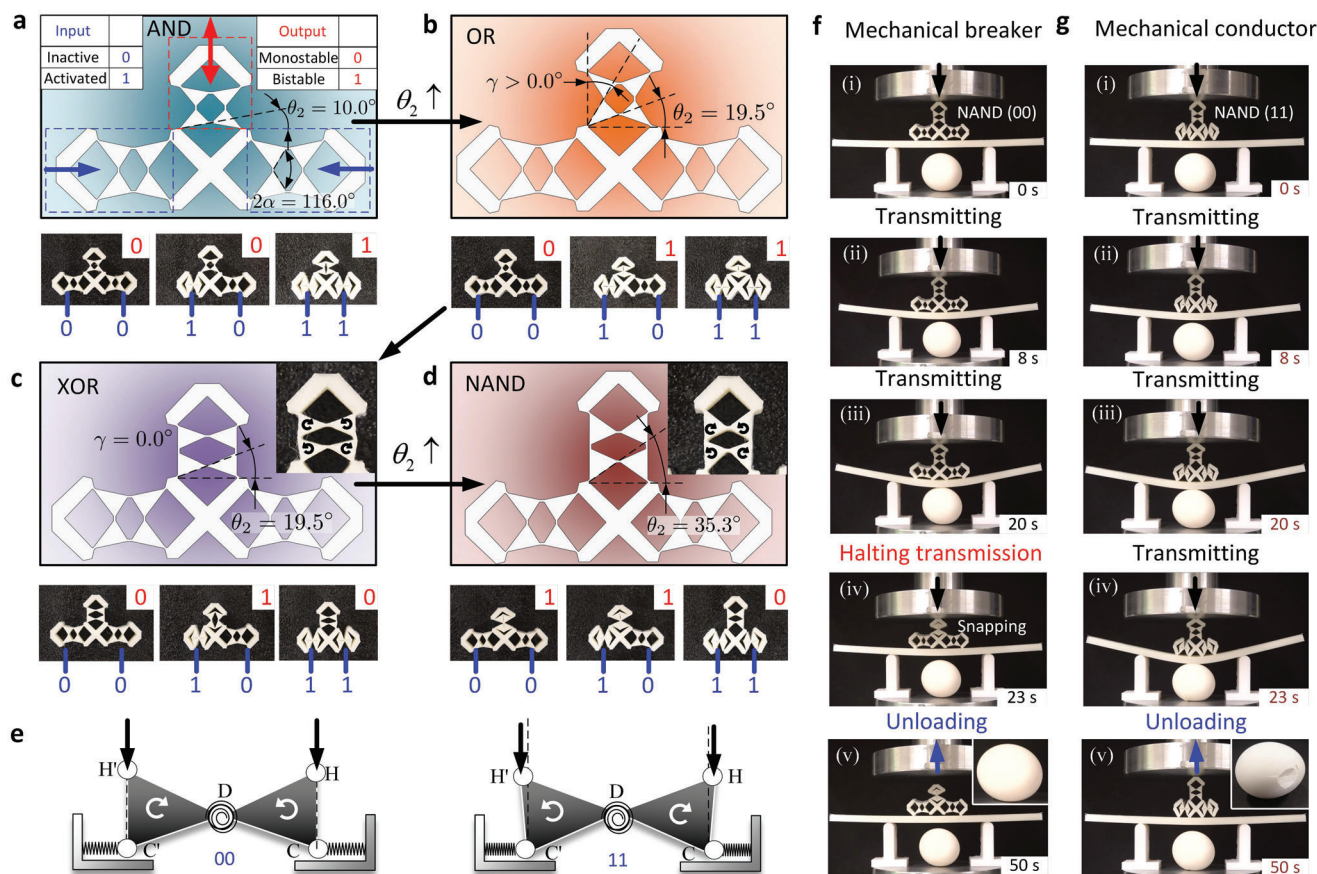


Figure 3. Demonstration of a) “AND”, b) “OR”, c) “XOR”, d) “NAND” mechanical logic gates, and the approach for designing them through rational tuning of their geometry parameters. e) Discretized model illustrating why the output architecture of the “XOR” and “NAND” gates cannot transition to its second state if both sides are activated. Use of “NAND” gate as either f) mechanical breaker with input “00”, or g) conductor with “11” input to respectively cease or keep motion transmission upon reaching a threshold (5mm). If the input is “01” or “10”, the “NAND” gate behaves as a mechanical breaker similar to the state “00”.

ment load of 12 mm is applied to the loading head and then transmitted to the elastic beam via the “NAND” gate. If the input is “00”, the “NAND” gate and the elastic component deform as a whole and deliver the displacement from the loading head downstream (Figure 3f-i to iii). Once the displacement reaches the threshold of about 5 mm, the bistable “NAND” gate snaps to its second state, and simultaneously, the elastic beam bounces back to a slightly-deformed configuration, breaking off the mechanical circuit (Figure 3f-iv), and thus halting the displacement transmission to the target object (Figure 3f-v). In contrast, if the input is “11”, the “NAND” gate is monostable and can deliver the displacement from the loading head all the way down where the target object lies, a behavior representative of a mechanical conductor (Movie S6, Supporting Information). The functionality here presented as a mechanical breaker and conductor can be embedded into other motion-transmission systems that require displacement monitoring. In addition, since our mechanical logic gate outputs monostability/bistability, the output end of one logic gate can serve as an independent input for the next level, a characteristic that can be integrated into a hierarchical architecture to implement more complex logical operations.

5. Multi-Response 3D Metamaterial

In Figure 2, we have demonstrated that our 2D metamaterial has one activation direction and can deliver two distinct mechanical responses in the other direction. We now extend the idea to 3D by incorporating two directions of activation. This strategy enables to generate a 3D metamaterial that can combine monotonic, monostable snap-through, and bistable snap-through responses within one architecture. **Figure 4a** shows a representative 3D unit cell in its distinct topological states and the corresponding periodic metamaterial. The 3D unit cell is built by orthogonally merging two identical 2D unit cells, hence providing two normal directions of activation (blue arrows in Figure 4a). We manufactured a truncated $1 \times 1 \times 2$ structure and tested its response in the z-direction in the state with no activation (“00”), the state with one direction being activated (“01” or “10”), and the state with both directions activated (“11”). Due to the symmetry of the 3D unit cell, the states “01” and “10” have similar mechanical characteristics. As shown in Figure 4b, through a rational selection of the geometry parameters (Section SIV, Supporting Information), the building block can deliver monotonic, monostable snap-through, and bistable snap-through in the “00”, “01”,

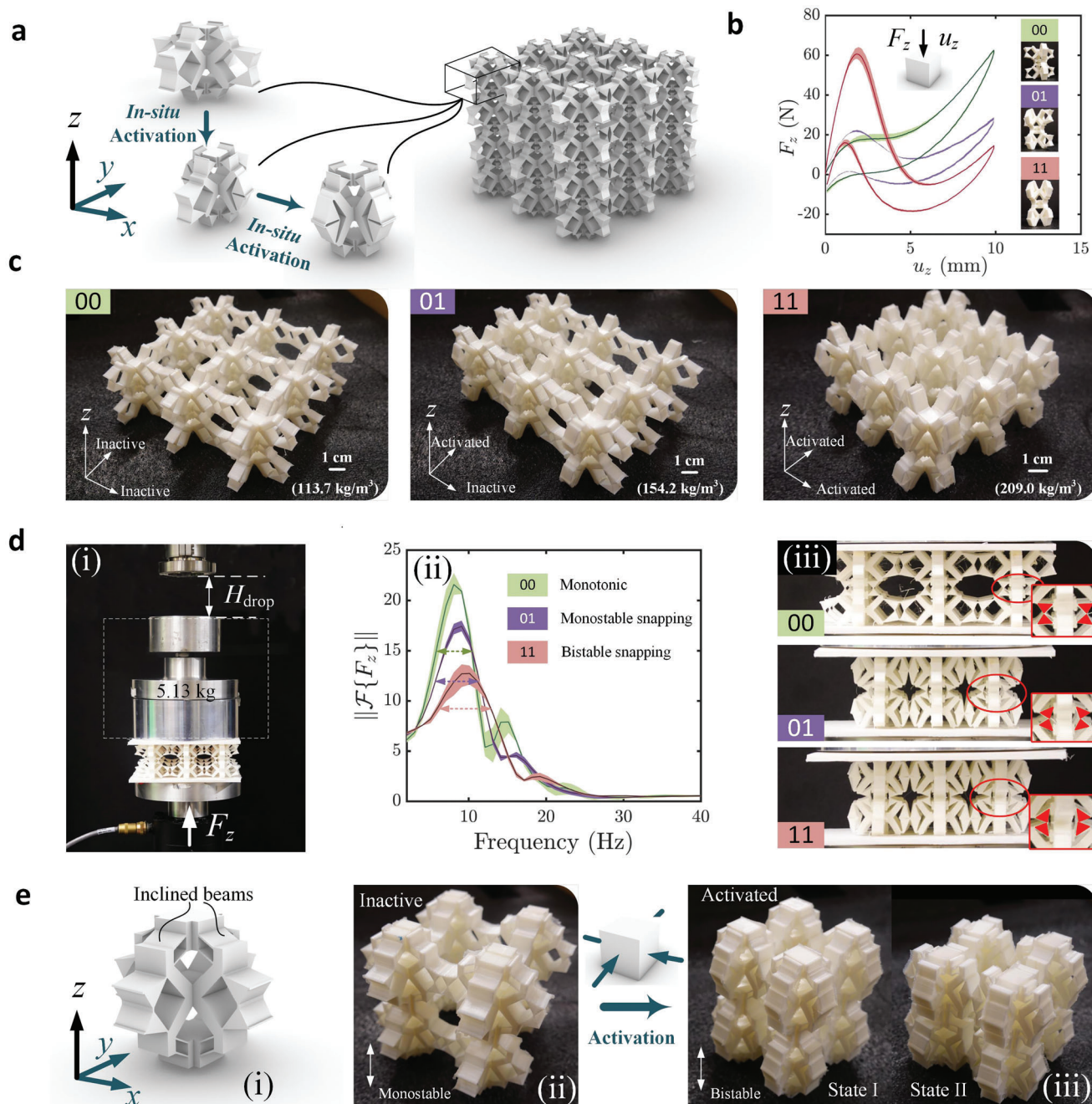


Figure 4. a) Illustration of 3D multi-response unit cell in its distinct topological states (left) and corresponding periodic metamaterial (right). b) Three types of force–displacement responses of a truncated building block in its distinct states. c) Finite-period tessellation of truncated building block and its activated configurations. d) Low-velocity drop test on a sandwich panel comprising the reprogrammable tessellation, where $H_{drop} = 54$ mm (i); (ii) frequency response of reaction force (F_z) in drop test showing that the panel can exhibit dissimilar levels of energy dissipation with reprogrammable damping ratio and peak frequency; (iii) deformed configuration of the inclusion elucidating that the activated state can dissipate energy more efficiently due to the larger rotation of the local triangles. e) Extension of our concept to beam-type architectures capable of also attaining a robust activation from monostable to bistable.

and “11” states respectively, attesting that the larger the number of activated directions, the more sizeable the snap-through behavior.

Given our 3D metamaterial can be activated to exhibit three types of force–displacement relations, each with its own distinct

degree of hysteresis, we now demonstrate its promise in developing a reprogrammable sandwich structure with in situ adjustable energy dissipation. Figure 4c illustrates a finite-period structure tessellated by the truncated building block (inset in Figure 4b) in a $3 \times 3 \times 1$ manner. Figure 4c shows the corresponding acti-

vated states. The finite-period structure can be accommodated in between two polylactic acid plates to form a sandwich panel. A low-velocity drop test is performed to investigate the energy attenuation capacity of the sandwich panel in three distinct states (Figure 4d-i). We monitor the reaction force (F_z) versus time until its fluctuation is negligible and then transform the signal in the time domain to the frequency domain. As shown in Figure 4d-ii, with more directions being activated, the peak value of the frequency response substantially reduces. More specifically, the peak responses in states “01” and “11” are about 80% and 57% of that in the state “00”. Furthermore, from the state “00” to “01” and then “11”, the half power bandwidth of the frequency response gradually increases (dashed arrows in Figure 4d-ii), thus implying a higher effective damping ratio endowed by the snapping constituents and the viscoelasticity of the base material. This signifies that the activated metamaterial can dissipate the input energy in a shorter time, and the energy is mainly dissipated via the rotation of the triangles (red solid triangles in Figure 4d-iii). The activated metamaterial (states “01” and “11”) undergoes a larger local rotation than the inactive metamaterial (state “00”), and hence can dissipate energy more efficiently. Moreover, the response peak slightly shifts toward a higher-frequency regime once the metamaterial has been activated, a phenomenon that can be attributed to the augmentation of the metamaterial incremental stiffness post-activation (see the initial slope of the three curves in Figure 4b). By virtue of the reprogrammable capacity of energy dissipation, our metamaterial is especially suitable for shock absorbers with adjustable wave transmittance and for multifunctional sport equipment, for example, sneakers, calling to satisfy requirements imposed by different sport activities.

We finally showcase the generality of our concept and demonstrate that activating bistability via contact-induced topological transformation is not limited to the architecture we discussed here. Rather it can be applied to other structural concepts. For example, we can replace the architecture along the responding direction with inclined beams while keeping the architecture along two activation directions unchanged (Figure 4e-i). The resulting metamaterial can achieve similar mechanical performance to the metamaterial in Figure 4a, thus offering both activatable bistability and reprogrammable energy dissipation capacity (Figure 4e-ii and -iii). Shell-type architectures can also be accommodated into our concept so as to gain not only switchable bistability, but also a high stiffness-to-weight ratio.^[45] This demonstrates the versatility of our concept, which provides a platform to design topology transformable metamaterials with reprogrammable mechanical characteristics.

6. Conclusion

We have introduced a class of multistable mechanical metamaterials with in situ activatable snap-through capacity. Through a combination of theoretical analysis, numerical simulations, and experiments, we have demonstrated how the snap-through instability in one principal direction can be reprogrammed on demand by altering the topological state of the metamaterial along the other principal axes. We have unveiled that this process is governed by a contact-induced topology transformation that enhances the geometry incompatibility and confinement stiffness of the metamaterial constituents. As a result, the mechanical

response can be switched in situ from monotonic to monostable/bistable snap-through as required by the application, hence demonstrating an unprecedented level of versatility in delivering distinct functionalities post-fabrication.

Since our metamaterial can be activated in situ to exhibit both positive and negative incremental stiffness, it has resolved the limitation of existing snapping metamaterials unable to perform in applications where a negative incremental stiffness is deleterious, such as when there is a need to transmit a force at a large strain. The multi-response nature of our metamaterial prior to and post-activation promises a broad range of applications including sandwich panels with reprogrammable energy dissipation capacity as we demonstrated, mechanical logic gates for system control, multifunctional sneakers, and vibration isolators with adjustable resonance frequency. Lastly, the approach of integrating internal contact and multistability to achieve topological transformation can be harnessed to reprogram the Poisson's ratio, the acoustic band structure and other mechanical properties.

7. Experimental Section

Sample Fabrication: The 2D finite-period structures in Figure 2 were manufactured by Anycubic Vyper (Anycubic, China) via the Fused Deposition Modeling out of the Anycubic White TPU filament. The 3D metamaterial samples in Figure 4 were assembled by planar parts (FDM, Anycubic White TPU) via a sleeve connection and adhesion. More details about the fabrication could be found in Supporting Information.

Uniaxial Compression Test: The compression tests on the 2D samples (Figure 2) were performed under a displacement-controlled load with a rate of 0.5 mm s^{-1} (MTS machine, MTS Systems Corporation, Eden Prairie, Minnesota, US). The compression tests on the 3D metamaterial samples (Figure 4b) were conducted with a 0.4 mm s^{-1} load (Bose ElectroForce 3510, Bose Corporation, Framingham, Massachusetts). The boundaries of the samples were anchored to the test machine via ductile tape. For each specimen, we perform the loading-unloading test 3 times and obtain the average response and the experimental uncertainty range. In Movies (Supporting Information), to better elucidate the bistability of the activated samples, we use an unanchored condition.

Low-Velocity Drop Test: Bose ElectroForce 3510 was used to conduct the drop test. The sandwich panel was placed on a rigid support, where a sensor was embedded to capture the reaction force F_z . The weight was released at a height of 54.0 mm. The force signal with a total time elapse of 20 s was recorded at a sampling frequency of 102 Hz. For the finite-period structure in each of its stable states, we perform the drop test 3 times and obtain the average response and the experimental uncertainty range.

Supporting Information

Supporting Information is available from the Wiley Online Library or from the author.

Acknowledgements

D.P. acknowledges financial support from the Canada Research Chairs Program and the Natural Sciences and Engineering Research Council of Canada. L.W. acknowledges financial support from the China Scholarship Council (202006280037).

Note: Punctuation typos in phrases x -, y -, z -direction, γ -response, and force–displacement were corrected on September 7, 2023, after initial publication online.

Conflict of Interest

The authors declare no conflict of interest.

Data Availability Statement

The data that support the findings of this study are available from the corresponding author upon reasonable request.

Keywords

in situ reprogrammability, mechanical metamaterials, multistability, snap-through instability, topological transformation

Received: February 4, 2023

Revised: April 17, 2023

Published online: June 30, 2023

-
- [1] D. M. Kochmann, K. Bertoldi, *Appl. Mech. Rev.* **2017**, 69, 050801.
- [2] M. Gomez, D. E. Moulton, D. Vella, *Nat. Phys.* **2017**, 13, 142.
- [3] C. F. Ng, S. A. Clevenson, *J. Aircraft* **1991**, 28, 275.
- [4] S. Krylov, B. R. Ilic, D. Schreiber, S. Seretensky, H. Craighead, *J. Micromech. Microeng.* **2008**, 18, 055026.
- [5] Y. Forterre, J. M. Skotheim, J. Dumais, L. Mahadevan, *Nature* **2005**, 433, 421.
- [6] Y. Cao, M. Derakhshani, Y. Fang, G. Huang, C. Cao, *Adv. Funct. Mater.* **2021**, 31, 2106231.
- [7] A. Pal, V. Restrepo, D. Goswami, R. V. Martinez, *Adv. Mater.* **2021**, 33, 2006939.
- [8] K. Bertoldi, V. Vitelli, J. Christensen, M. Van Hecke, *Nat. Rev. Mater.* **2017**, 2, 17066.
- [9] Y. Chi, Y. Li, Y. Zhao, Y. Hong, Y. Tang, J. Yin, *Adv. Mater.* **2022**, 34, 2110384.
- [10] T. Frenzel, C. Findeisen, M. Kadic, P. Gumbsch, M. Wegener, *Adv. Mater.* **2016**, 28, 5865.
- [11] A. Rafsanjani, A. Akbarzadeh, D. Pasini, *Adv. Mater.* **2015**, 27, 5931.
- [12] F. Pan, Y. Li, Z. Li, J. Yang, B. Liu, Y. Chen, *Adv. Mater.* **2019**, 31, 1900548.
- [13] S. Shan, S. H. Kang, J. R. Raney, P. Wang, L. Fang, F. Candido, J. A. Lewis, K. Bertoldi, *Adv. Mater.* **2015**, 27, 4296.
- [14] K. Fu, Z. Zhao, L. Jin, *Adv. Funct. Mater.* **2019**, 29, 1901258.
- [15] T. A. Hewage, K. L. Alderson, A. Alderson, F. Scarpa, *Adv. Mater.* **2016**, 28, 10323.
- [16] J. R. Raney, N. Nadkarni, C. Daraio, D. M. Kochmann, J. A. Lewis, K. Bertoldi, *Proc. Natl. Acad. Sci.* **2016**, 113, 9722.
- [17] L. Jin, R. Khajehtourian, J. Mueller, A. Rafsanjani, V. Tournat, K. Bertoldi, D. M. Kochmann, *Proc. Natl. Acad. Sci.* **2020**, 117, 2319.
- [18] G. Librandi, E. Tubaldi, K. Bertoldi, *Nat. Commun.* **2021**, 12, 3454.
- [19] B. Haghpanah, L. Salari-Sharif, P. Pourrajab, J. Hopkins, L. Valdeit, *Adv. Mater.* **2016**, 28, 7915.
- [20] Z. Meng, M. Liu, H. Yan, G. M. Genin, C. Q. Chen, *Sci. Adv.* **2022**, 8, eabn5460.
- [21] T. Chen, M. Pauly, P. M. Reis, *Nature* **2021**, 589, 386.
- [22] Y. Jiang, L. M. Korpas, J. R. Raney, *Nat. Commun.* **2019**, 10, 128.
- [23] T. Mei, Z. Meng, K. Zhao, C. Q. Chen, *Nat. Commun.* **2021**, 12, 7234.
- [24] L. S. Novelino, Q. Ze, S. Wu, G. H. Paulino, R. Zhao, *Proc. Natl. Acad. Sci.* **2020**, 117, 24096.
- [25] T. Chen, J. Mueller, K. Shea, *Sci. Rep.* **2017**, 7, 45671.
- [26] T. Chen, O. R. Bilal, K. Shea, C. Daraio, *Proc. Natl. Acad. Sci.* **2018**, 115, 5698.
- [27] C. Qiao, L. Liu, D. Pasini, *J. Mech. Phys. Solids* **2020**, 141, 103959.
- [28] J. A. Faber, J. P. Udani, K. S. Riley, A. R. Studart, A. F. Arrieta, *Adv. Sci.* **2020**, 7, 2001955.
- [29] K. Liu, P. P. Pratapa, D. Misseroni, T. Tachi, G. H. Paulino, *Adv. Mater.* **2022**, 34, 2107998.
- [30] A. Rafsanjani, D. Pasini, *Extreme Mech. Lett.* **2016**, 9, 291.
- [31] S. Li, H. Fang, S. Sadeghi, P. Bhovad, K.-W. Wang, *Adv. Mater.* **2019**, 31, 1805282.
- [32] N. Nayakanti, S. H. Tawfik, A. J. Hart, *Extreme Mech. Lett.* **2018**, 21, 17.
- [33] X. Zheng, K. Uto, W.-H. Hu, T.-T. Chen, M. Naito, I. Watanabe, *Appl. Mater. Today* **2022**, 29, 101662.
- [34] Y. Zhang, M. Velay-Lizancos, D. Restrepo, N. D. Mankame, P. D. Zavattieri, *Matter* **2021**, 4, 1990.
- [35] X. Lin, F. Pan, K. Yang, J. Guan, B. Ding, Y. Liu, K. Yang, B. Liu, Y. Chen, *Adv. Funct. Mater.* **2021**, 31, 2101808.
- [36] D. Melancon, B. Gorissen, C. J. Garcia-Mora, C. Hoberman, K. Bertoldi, *Nature* **2021**, 592, 545.
- [37] X. Zhang, Y. Wang, Z. Tian, M. Samri, K. Moh, R. M. McMeeking, R. Hensel, E. Arzt, *Sci. Adv.* **2022**, 8, eadd4768.
- [38] C. Coulais, A. Sabbadini, F. Vink, M. van Hecke, *Nature* **2018**, 561, 512.
- [39] B. Deng, A. Zareei, X. Ding, J. C. Weaver, C. H. Rycroft, K. Bertoldi, *Adv. Mater.* **2022**, 34, 2206238.
- [40] M. Gomez, D. E. Moulton, D. Vella, *J. Mech. Phys. Solids* **2019**, 124, 781.
- [41] M. Santer, *Int. J. Solids Struct.* **2010**, 47, 3263.
- [42] T. Liu, Y. Chen, L. Liu, Y. Liu, J. Leng, L. Jin, *Extreme Mech. Lett.* **2021**, 49, 101477.
- [43] H. Zhang, J. Wu, D. Fang, Y. Zhang, *Sci. Adv.* **2021**, 7, eabf1966.
- [44] Z. Meng, W. Chen, T. Mei, Y. Lai, Y. Li, C. Chen, *Extreme Mech. Lett.* **2021**, 43, 101180.
- [45] S. C. Han, J. W. Lee, K. Kang, *Adv. Mater.* **2015**, 27, 5506.